



## Whitecapping and wave field evolution in a coastal bay

R. P. Mulligan,<sup>1</sup> A. J. Bowen,<sup>1</sup> A. E. Hay,<sup>1</sup> A. J. van der Westhuysen,<sup>2,3</sup> and J. A. Battjes<sup>2</sup>

Received 9 August 2007; accepted 9 October 2007; published 11 March 2008.

[1] Evolution of the wave field in a coastal bay is investigated, by comparison between field observations and numerical simulations using a spectral wave model (Simulating WAVes Nearshore (SWAN)). The simulations were conducted for the passage of an extratropical storm, during which surface elevation spectra were bimodal owing to local wind-sea generation and swell propagation into the bay. SWAN was run in stationary and nonstationary mode for two whitecapping source term formulations. The first was developed by Komen et al. (1984) and is dependent on spectrally averaged wave steepness, and thus includes swell in the calculation of whitecapping dissipation and typically overestimates wind sea in the presence of swell. The second, proposed by van der Westhuysen et al. (2007), estimates whitecapping of wind sea locally in the wave spectrum and is not coupled to swell energy. This formulation reproduced the magnitude and shape of the observed wind-sea spectral peak much better than the previous formulation. Whitecapping dissipation rates have been estimated from observations, using the equilibrium range theory developed by Phillips (1985), and are well correlated with both wind speed and acoustic backscatter observations. These rates agree with SWAN estimates using the spectrally local expression, and provide additional physical validation for the whitecapping source term.

**Citation:** Mulligan, R. P., A. J. Bowen, A. E. Hay, A. J. van der Westhuysen, and J. A. Battjes (2008), Whitecapping and wave field evolution in a coastal bay, *J. Geophys. Res.*, 113, C03008, doi:10.1029/2007JC004382.

### 1. Introduction

[2] The wave field at the ocean surface is generally composed of both swell (0.05–0.30 Hz) generated by remote winds and wind sea (0.30–1.00 Hz) generated by local winds. In coastal areas, swell undergoes significant transformations by refraction, shoaling and breaking. Local winds blowing over coastal waters can generate wind sea that is limited by whitecapping dissipation, but can dominate the wave field in areas that are protected from swell. Numerical wave models are very useful for evaluating wave conditions near the coast, allowing for simulation of the wave field at higher spatial resolution than could ever be sampled in nature. It is the purpose of this study to evaluate whitecapping dissipation formulations in a state-of-the-art wave model, by comparison with wave observations that resulted from combined swell and wind sea in a coastal bay.

[3] There have been numerous investigations of the whitecapping dissipation process. *Hasselmann et al.* [1973] developed a pulse-based whitecapping formulation that is the basis for the *Komen et al.* [1984] expression, widely used in wave models today. However, it has been noted in several studies that for combined swell and wind

sea, this formulation overpredicts the total wave energy and spectral distribution. *Booij et al.* [2001] discuss the validity of the *Komen et al.* [1984] whitecapping formulation in the absence of swell, and test whitecapping modifications when swell is present. *Rogers et al.* [2002] discuss the artificial impact of swell energy on wind-wave growth. They conclude that the erroneous behavior is due to the dissipation term being strongly weighted by the spectral mean frequency, and recommend a revisit of the *Komen et al.* [1984] investigation. *van der Westhuysen et al.* [2007] address this shortcoming directly and remove the spurious influence of swell on wind sea, by removing the dependence of spectral-mean wave steepness from the description of the whitecapping process. Whitecapping has also been examined by estimating the wave energy dissipation rates from observations of surface elevation spectra. This is achieved by *Hanson and Phillips* [1999], who examine the effects of swell on local wind-wave growth. *Felizardo and Melville* [1995] estimate dissipation rates using models of both *Komen et al.* [1984] and *Phillips* [1985], and correlate results with observations of wind speed, wave amplitude and ambient sound pressure.

[4] SWAN (Simulating WAVes Nearshore) is a spectral wave model developed by *Booij et al.* [1999] that is widely used to simulate wave conditions in coastal areas. *Ris et al.* [1999] provide spectral verification for the model for stationary storms in coastal regions along the Netherlands coast. *Ou et al.* [2002] estimate cyclonic wind fields and use SWAN to simulate typhoon wave conditions over a regional domain near Taiwan, comparing model results to observed bulk wave statistics. *Rogers et al.* [2002] describe white-

<sup>1</sup>Department of Oceanography, Dalhousie University, Halifax, Nova Scotia, Canada.

<sup>2</sup>Environmental Fluid Mechanics Section, Faculty of Civil Engineering and Geosciences, Delft University of Technology, Delft, Netherlands.

<sup>3</sup>Now at WL|Delft Hydraulics, Delft, Netherlands.

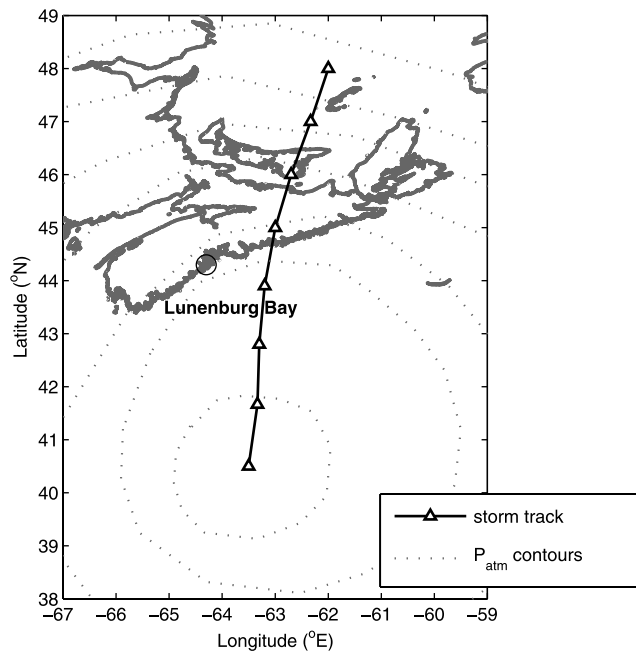


**Figure 1.** Map showing location of Lunenburg Bay in Nova Scotia and the track of the combined low-pressure system, including extratropical storm Nicole. Atmospheric pressure contours are shown for 1800 UTC 11 October 2004, the inner contour is 992 mbar and the contour interval is 4 mbar. Triangles show the location of the storm center and are spaced at 6-hour intervals (data from nomads.ncdc.noaa.gov).

capping as the “least understood” wave process and investigate a fundamental problem in the form of the whitecapping term in SWAN, causing dissipation to be very sensitive to the presence of swell. Rogers *et al.* [2006] tested SWAN performance for stationary and nonstationary runs, over cascading domain scales in southern California. They found that primary contributors to model error, when compared to buoy data, were inaccuracy in the representation of wind forcing, inaccuracy in the directional distribution of wave energy at open boundaries and the relatively poor prediction of wind-sea growth/dissipation using stationary computations.

[5] During the passage of an extratropical storm, Lunenburg Bay, Nova Scotia, was exposed to a wide range of wave conditions, the combined influence of both incoming swell and strong winds. The wind direction in the bay rotated through time in association with the proximity of the storm center, causing fetch limitations and duration limitations to wind sea. The ability of the SWAN model to simulate the wave conditions is tested, when driven by the various combinations of wind and swell conditions that occurred during the storm. Two whitecapping source terms are evaluated, by comparing the simulations with observations. The whitecapping formulations tested are available in SWAN. The Komen *et al.* [1984] formulation (denoted as KHH84 hereinafter) depends on the mean spectral steepness and is the default option in SWAN version 40.41. The recently proposed van der Westhuysen *et al.* [2007] formulation (denoted as WZB07 hereinafter) depends upon the

local spectral steepness and is included in SWAN version 40.51, released in August 2006.

[6] This paper is organized as follows: Section 2 presents a description of the study site, the storm event, the instruments and wave observations. Section 3 describes the SWAN model and the whitecapping formulations under consideration. Section 4 describes the model results, the boundary input and forcing conditions. Section 5 presents comparisons between observed data and model results for bulk wave statistics, spectra, source terms and dissipation rate estimates, highlighting differences between whitecapping formulations and providing a description of the evolution of the wave field. Conclusions are in section 6.

## 2. Observations

[7] The study site is Lunenburg Bay, on the southern shore of Nova Scotia, Canada, shown in Figure 1. It is approximately 8 km long, 4 km wide and has a typical depth of 10 m. The bathymetry is irregular and the bay is exposed to wave energy from the North Atlantic Ocean from easterly and southerly directions (Figure 2). Incident waves refract around an offshore island and encounter a shallow (2 to 5 m) rocky shoal near the center of the bay at the eastern side. South of the shoal a 20-m-deep channel penetrates the bay, near which several observation stations were located in 2004, shown in Figure 2. South of this channel, the headland shelters the coast from direct swell. Wave energy is attenuated toward the western end of the bay. The town of Lunenburg is located on the harbor at the northwest, and at the southwest the bay is connected to two small coves by a 200-m-wide tidal channel. Tidal circulation in Lunenburg Bay has been studied by Sturley and Bowen [1996] and Sheng and Wang [2004] and is a topic of active research.

[8] Wave and current data have been collected in Lunenburg Bay since 2002, part of the real-time coastal observing system set up at Dalhousie University under the Centre for Marine Environmental Prediction ([www.cmep.ca](http://www.cmep.ca)). Wave observations in 2004 were made using several instruments, listed in Table 1 and shown in Figure 2. The instruments included a directional wave buoy (*D*), pressure sensors (*P1*, *P2*), and acoustic profiling instruments capable of measuring surface waves (*A1*, *A2*, *A3*). Figure 3 shows significant wave height ( $H_s$ ) measured at *D*, *A1*, *A2*, and *A3* in October 2004, during which named storms Lisa and Nicole occurred.

[9] Nicole formed as a northward-moving subtropical storm near Bermuda on 10 October 2004. On 11 October, it underwent extratropical transition and combined with a larger midlatitude low-pressure system south of Nova Scotia. The storm system passed close to the coast of Nova Scotia (Figure 1) on 11–12 October, yearday (YD) 285–286, providing large swell, strong winds and heavy rainfall. Wind data observed at three stations in Lunenburg Bay (*W*, *P1*, *P2*), are shown in Figure 4 for the event, and the range in observed water levels during the storm was 1.44 m (Figure 4d).

### 2.1. Directional Wave Buoy

[10] The directional waverider (site *D*, Figure 2) is a surface heave-pitch-roll buoy that sampled at a rate of 1.28 Hz. Auto- and cross-spectral densities of the heave and surface slopes were estimated using a Hanning window with 50% overlap. The Maximum Entropy Method (MEM)

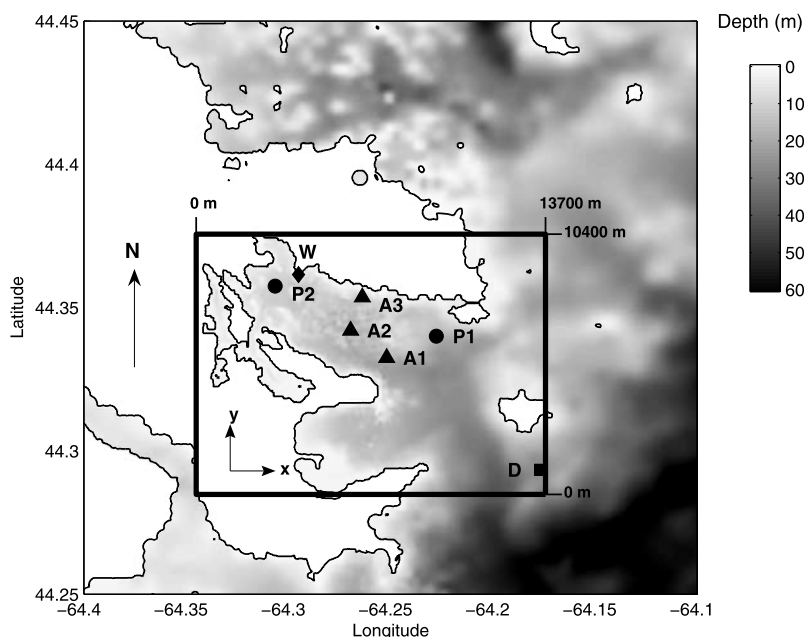


**Figure 2.** Lunenburg Bay model domain, bathymetry, and instrument locations in October 2004. *D* denotes directional wave buoy, *A* denotes acoustic bottom pod, *P* denotes surface meteorological buoy and bottom pod with pressure sensor, and *W* denotes a land-based meteorological station. Depths are relative to the low water tidal datum.

was used to estimate directional spectra at the buoy. This method, described by *Lygre and Krogstad* [1986] and *Krogstad* [1991], uses the measurement of surface heave ( $\eta$ ), two orthogonal horizontal measurements of surface slopes ( $\frac{d\eta}{dx}$ ,  $\frac{d\eta}{dy}$ ) and the wave number  $k$ , estimated using linear wave theory, to construct the directional spreading function  $D(\sigma, \theta)$ . The use of three measurements at one location allows the first two pairs ( $n = 1, 2$ ) of complex Fourier coefficients ( $a_n, b_n$ ) to be estimated. The directional spreading function, when expanded into a Fourier series for a discrete process, is the sum of cosine and sinusoidal components multiplied by  $a_n$  and  $b_n$ . The MEM estimate maximizes entropy of  $D(\sigma, \theta)$  and ensures that it is a positive function. According to *Lygre and Krogstad* [1986], this represents the most probable estimate of the distribution given only the first two pairs of Fourier coefficients.

[11] The two-dimensional energy spectrum  $E(\sigma, \theta)$  is given by the product of the one-dimensional energy spectrum  $E(\sigma)$  for surface heave and the directional spreading function  $D(\sigma, \theta)$ , thus describing wave energy in frequency and directional space,

$$E(\sigma, \theta) = E(\sigma)D(\sigma, \theta), \quad (1)$$

where

$$\int_0^{2\pi} D(\sigma, \theta) d\theta = 1. \quad (2)$$

[12] The directional spectrum at the waverider buoy is shown in Figure 5 at selected times during extratropical storm Nicole. Bulk wave statistics were determined from

the directional spectrum, including the significant wave height  $H_s$ , peak wave period  $T_p$ , mean absolute wave period  $T_{m01}$ , mean wave direction  $\theta_m$  and mean directional spread  $s_m$  (Figures 4e–4g).

## 2.2. Acoustic Wave Observations

[13] Three acoustic Doppler profiling instruments were located in Lunenburg Bay, shown in Figure 2 and summarized in Table 1. These included a Nortek AWAC (site *A2*), and two RDI Waves ADCPs (sites *A1*, *A3*). The AWAC operated at an acoustic frequency of 1 MHz and has four transducers oriented with one beam pointing vertically upward and three slanted at  $25^\circ$  to the vertical. It was configured to sample at 2.00 Hz for pressure and velocity observations and at 4.00 Hz for acoustic surface tracking, and burst sampled for 17 min every 20 min. The Waves ADCPs both operated at an acoustic frequency of 1.2 MHz and have four transducers, all slanted at  $20^\circ$  to the vertical. They were configured to sample at 2.00 Hz for pressure, velocity and surface echo observations. *A1* burst sampled

**Table 1.** Wave Instruments in Lunenburg Bay in October 2004

Name	Type	h	$f_s$
<i>Surface Buoy</i>			
<i>D</i>	DataWell directional waverider buoy	30 m	1.28 Hz
<i>Bottom-Mounted Pressure Sensors</i>			
<i>P1</i>	Seabird pressure sensor	13 m	0.62 Hz
<i>P2</i>	Seabird pressure sensor	10 m	0.62 Hz
<i>Bottom-Mounted Acoustic Sensors</i>			
<i>A1</i>	RDI Waves ADCP (1.2 MHz)	19 m	2.00 Hz
<i>A2</i>	Nortek AWAC (1.0 MHz)	21 m	4.00 Hz
<i>A3</i>	RDI Waves ADCP (1.2 MHz)	10 m	2.00 Hz

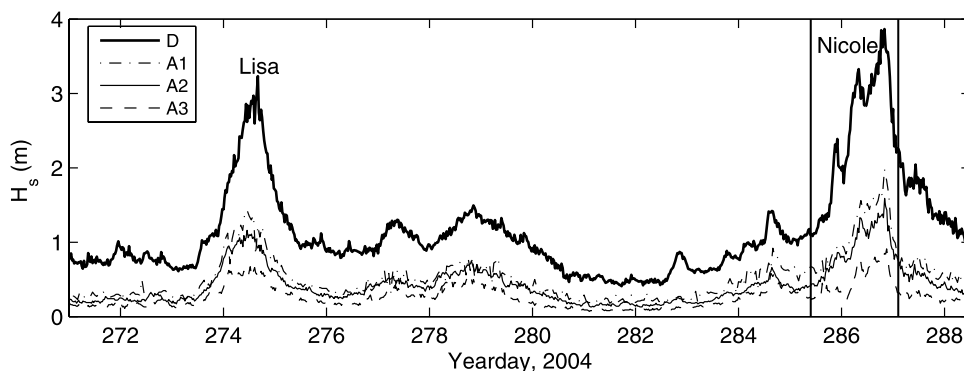


**Figure 3.** Wave observations for 29 September to 15 October 2004, at the directional waverider buoy (*D*) outside the bay and three acoustic bottom pods (*A1*, *A2*, and *A3*) inside the bay. Swell events from named storms Hurricane Lisa and extratropical storm Nicole occurred within this period. Vertical lines indicate the model simulation period.

for 20 min every 60 min, and *A3* burst sampled for 20 min every 30 min. Surface elevation spectra were estimated using the proprietary software for each instrument. All three instruments made velocity observations in the water column using a 0.5-m bin size. However, at *A3* the farthest bins from the instrument (near-surface) were incorrectly set,

leading to a loss of information on the sea surface location and surface waves at high water levels. Therefore observations from *A1* and *A2* are primarily used to compare to model results in later sections.

[14] Acoustic instruments, such as the AWAC or Waves ADCPs, estimate surface elevation spectra on the basis of

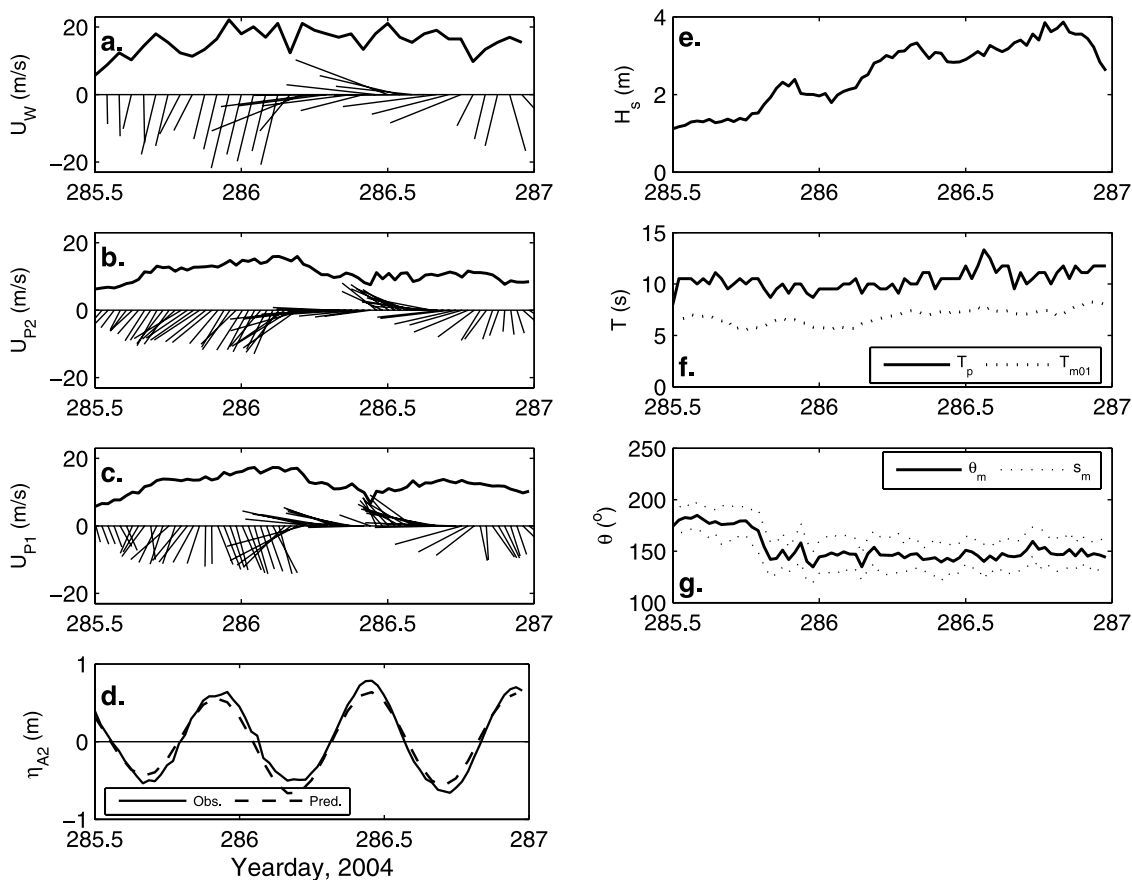


**Figure 4.** Time series of wind velocity, water level, and wave observations. Wind speed, adjusted to 10 m, is shown by the dark line in Figures 4a–4c, with stick vectors showing direction relative to true north: (a) hourly wind at land station *W*, (b) half-hourly winds at surface buoy *P2*, and (c) half-hourly wind at surface buoy *P1*. (d) Observed and predicted tidal water level change  $\eta$  from mean at bottom pod *A2*. Bulk wave statistics observed at the waverider buoy (site *D*): (e) significant wave height, (f) peak and mean wave period, and (g) mean wave direction and directional spread.

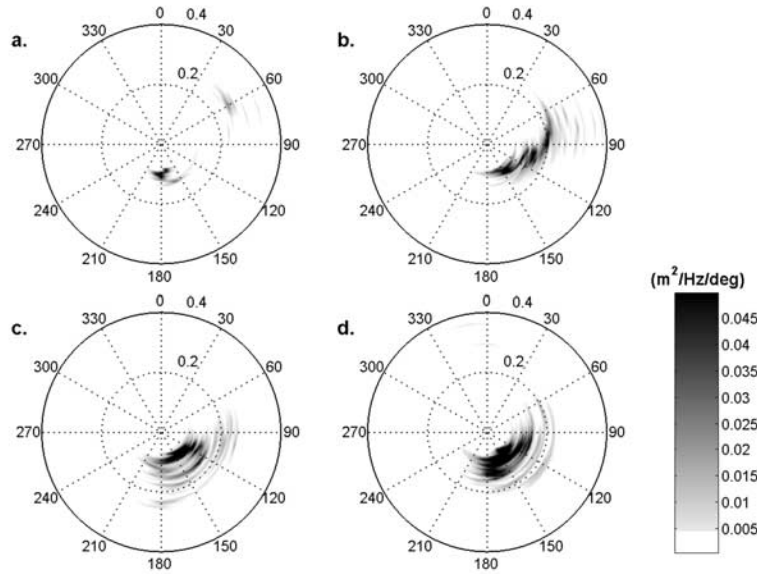


**Figure 5.** Selected observations at 9-hour intervals of surface wave directional spectra  $E$  ( $\text{m}^2/\text{Hz}/\text{deg}$ ) at the wave buoy (site  $D$ ): (a) YD 285.73,  $H_s = 1.4$  m; (b) YD 286.10,  $H_s = 2.1$  m; (c) YD 286.48,  $H_s = 2.8$  m; and (d) YD 286.85,  $H_s = 3.6$  m. Directions are in degrees relative to true north.

measurements of pressure, velocity and acoustic range to the sea surface. These three methods for observation of wave processes differ fundamentally. The pressure is observed using a pressure sensor at the depth of the instrument. These observations are frequency-limited and depend on the instrument depth, since the wave-induced oscillatory pressure signal measured at the sea bed in water depth  $h$  is proportional to  $1/\cosh(kh)$ . Consequently, wave energy at higher frequencies (i.e., over 0.30 Hz) is not detected when the instrument is placed in a deep location (i.e.,  $>10$  m) and a significant portion of the spectrum (i.e., wind sea) is not observed. Velocity observations are made by each slanted beam. Wave directional spectra are estimated using auto- and cross-spectra of the orthogonal velocity components. Owing to acoustic beam spreading and the physical separation distance between beams, the velocity observation method results in a limiting frequency. This frequency limit, which is dependent on  $h$ , can exclude wind-sea components from observations. The acoustic range to the sea surface, or the echo-located surface, is a direct measurement of surface displacement. This measurement has a frequency limit imposed by the beam footprint on the sea surface. For the instrument depths in this study, this was the best spectral measurement, including both swell and higher frequency wind-sea components. Surface elevation spectra from acoustic range observations are used in this paper to make comparisons with model predictions.

### 2.3. Pressure Sensors

[15] Pressure sensors in Lunenburg Bay at  $P1$  and  $P2$  (Figure 2) were located in mean depths of 13 and 10 m, respectively. The sensors collected pressure data continuously at a sampling rate of 0.62 Hz. Pressure spectral densities  $E_{pp}(\sigma)$  were estimated at the mean depth of each instrument, using a Hanning window with 50% overlap. Sea surface spectral densities  $E_{\eta\eta}(\sigma)$  were determined via mi-

gration of pressure spectral densities to the surface, using a transfer function derived from linear wave theory,

$$E_{\eta\eta}(\sigma) = \frac{E_{pp}(\sigma)}{\rho g} \frac{\cosh(kh)}{\cosh(k(z+h))}, \quad (3)$$

where  $h$  is the water depth and  $z$  is the instrument depth from mean sea level measured positive upward. This transfer function accounts for the frequency-dependent decay of the wave pressure signal with depth. The observations at  $P1$  and  $P2$  were limited by the sampling rate and were unable to measure wave-induced pressure fluctuations at higher frequencies associated with local wind sea (above 0.30 Hz), discussed in section 4.

### 3. SWAN Model and Whitecapping Formulations

[16] The SWAN model is a third-generation shallow-water spectral wave model that includes wave propagation, refraction due to currents and depth, generation by wind, dissipation (whitecapping, bottom friction, depth-induced breaking), and nonlinear wave-wave interactions [Booij *et al.*, 1999]. The model conserves wave action density  $N(\sigma, \theta)$ , the energy density  $E(\sigma, \theta)$  divided by the intrinsic frequency  $\sigma$ . The evolution of the wave field in SWAN is described by the action balance equation,

$$\frac{\partial}{\partial t} N + \frac{\partial}{\partial x} c_x N + \frac{\partial}{\partial y} c_y N + \frac{\partial}{\partial \sigma} c_\sigma N + \frac{\partial}{\partial \theta} c_\theta N = \frac{S_{tot}}{\sigma}, \quad (4)$$

which describes the local rate of change of action density in time ( $t$ ), and the propagation of action density in each dimension. Velocities  $c_x$  and  $c_y$  are spatial  $x$  and  $y$  components of the group velocity  $c_g$ , the speed at which wave action is transported. Here  $c_\theta$  and  $c_\sigma$  are rates of change of  $c_g$ , which describe the directional ( $\theta$ ) rate of

**Table 2.** SWAN Model Run Descriptions

Run	Whitecapping	Mode
KS	KHH84	stationary
WS	WZB07	stationary
KN	KHH84	nonstationary
WN	WZB07	nonstationary

turning and frequency ( $\sigma$ ) shifting due to changes in currents and water depth.

[17] Wave propagation described by the left-hand side of equation (4) is balanced by local changes to the wave spectrum described by energy density source terms  $S_{tot}$  on the right-hand side. The source terms describe wave generation by wind  $S_{in}$ , dissipation (whitecapping  $S_{wc}$ , bottom friction  $S_{fr}$ , depth-induced breaking  $S_{br}$ ) and nonlinear interactions (triads  $S_{nl3}$ , quadruplets  $S_{nl4}$ ), such that the total source term is

$$S_{tot} = S_{in} + S_{wc} + S_{nl4} + S_{fr} + S_{br} + S_{nl3}. \quad (5)$$

These processes all take part in the balance of wave action, to produce a wave field that is the result of the combined influences.

[18] Two whitecapping formulations have been used to simulate wave conditions in Lunenburg Bay. Each is an option within the most recent release of SWAN, and a detailed description is given by *van der Westhuysen et al.* [2007]. The KHH84 formulation is

$$S_{wc}(\sigma, \theta) = -C_{ds} \left(\frac{k}{\tilde{k}}\right)^q \left(\frac{\tilde{s}}{\tilde{s}_{PM}}\right)^r \tilde{\sigma} E(\sigma, \theta), \quad (6)$$

which is dependent on the mean frequency  $\tilde{\sigma}$ , the mean wave number  $\tilde{k}$  and the spectrally averaged steepness  $\tilde{s} = \tilde{k} \sqrt{E_{tot}}$ . The coefficient  $\tilde{s}_{PM}$  describes the mean, limiting wave steepness for the Pierson-Moskowitz spectrum, in the case of fully developed wave conditions.  $C_{ds}$ ,  $q$  and  $r$  are tuning parameters that are set to default values in SWAN ( $C_{ds} = 2.36 \times 10^{-5}$ ,  $q = 1$ ,  $r = 4$ ).

[19] The WZB07 formulation is a saturation-based dissipation expression, based on that of *Alves and Banner* [2003]. The original *Alves and Banner* [2003] expression has been reduced, by removing dependence on mean spectral steepness, to apply to whitecapping dissipation only and not to dissipation through interactions with long waves or turbulence. The WZB07 source term is expressed as,

$$S_{wc}(\sigma, \theta) = -C_{ds} \left[\frac{B(k)}{B_r}\right]^{p/2} \sqrt{gk} E(\sigma, \theta), \quad (7)$$

which is dependent on the local wave number  $k$  and independent of mean spectral steepness. Whitecapping occurs when  $B(k) > B_r$ , where  $B_r$  is the saturation threshold. Spectral saturation  $B(k)$ , defined in terms of dependence on wave number, is determined by

$$B(k) = \int_0^{2\pi} \frac{d\sigma}{dk} k^3 E(\sigma, \theta) d\theta = c_g k^3 E(\sigma). \quad (8)$$

Exponent  $p$  takes a functional form that is set to a constant  $p_o$  when  $B(k) > B_r$ . When there is no whitecapping,  $B(k) < B_r$  and  $p$  smoothly transitions to account for other (weaker) forms of dissipation such as turbulence and long-wave-short-wave interactions. SWAN defaults for tunable parameters are  $B_r = 1.75 \times 10^{-3}$  and  $C_{ds} = 5.0 \times 10^{-5}$ .

[20] The WZB07 whitecapping formulation was used in conjunction with a wind input source term  $S_{in}$  based on work by *Yan* [1987], refitted to observations of *Snyder et al.* [1981] and described by *van der Westhuysen et al.* [2007]. This wind input term is more accurate for young waves, differing from that of *Komen et al.* [1984] (also based on observations of *Snyder et al.* [1981]), which is used with the KHH84 whitecapping formulation. The different  $S_{in}$  formulations used in this study result in only minor differences in overall spectral energy levels (section 5.3). Wind input terms by both *Yan* [1987] and *Komen et al.* [1984] are completely local in frequency space, and momentum transfer to wind sea does not depend on the presence of swell.

#### 4. SWAN Simulations

[21] The model was implemented on a rectangular grid with bathymetry for Lunenburg Bay (Figure 2), covering an area of 13.7 km in the  $x$  direction and 10.4 km in the  $y$  direction with a resolution of  $\Delta x = \Delta y = 60$  m. Frequency space was resolved in 49 logarithmic bins from 0.03 to 3.00 Hz ( $\Delta\sigma/\sigma = 0.1$ ), and direction space was resolved in  $\Delta\theta = 10^\circ$  increments. Boundary conditions for incoming wave energy (swell) were expressed uniformly along the open boundaries (Figure 2), described by the MEM estimate (section 2.1) of directional spectra from the directional wave buoy located near the boundary. Physical processes including depth-induced breaking, bottom friction and nonlinear interactions were included, using default settings in SWAN. Water levels observed at A2 were input to the model, providing realistic time-varying water depth over the entire domain. The observed water level changes, shown in Figure 4 for the simulation period, are mainly tidal but also include surge associated with the extratropical storm. The peak surge was approximately 0.14 m, which was determined by the difference between observations and tidal predictions using WebTide [*Dupont et al.*, 2002].

[22] Four runs were conducted over the duration of the storm, listed in Table 2, in stationary and nonstationary mode for two whitecapping formulations. In stationary mode, the wave field is evolved with no limitations to the duration of wind-forcing. Each time step is treated as a separate computation, with no influence from the wave field of the previous time step. At least 30 iterations were conducted at each time step to ensure numerical convergence, and computations were conducted at 60-min intervals. In nonstationary mode, evolution of the wind-sea portion of the wave spectrum is limited by  $\Delta t$ . Time was included in the computation of the wave field, and the wave boundary conditions, wind forcing and water levels were updated at each step. A time step of  $\Delta t = 30$  min was selected owing to input data availability. Nonstationary runs were computationally faster than stationary runs, since

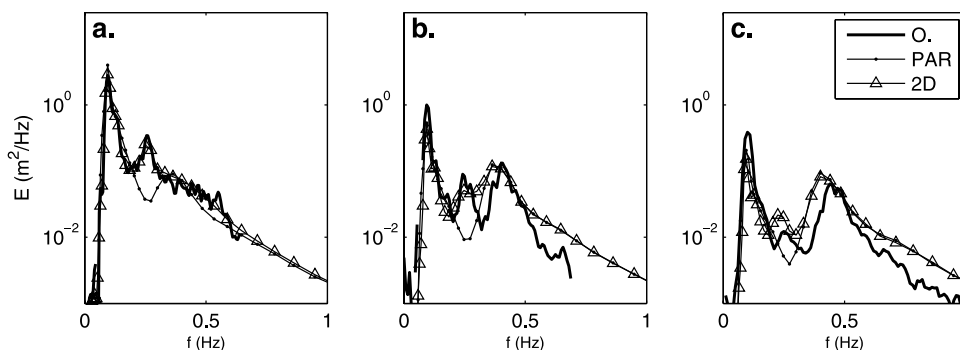


**Figure 6.** Comparison of surface elevation spectra for observations (thick line) and SWAN simulations (WN) using different boundary inputs: PAR is bulk wave statistics with JONSWAP spectral shape; 2D is observed directional spectra, at (a) site *D*, (b) site *A1*, and (c) site *A2* on YD 285.73 (11 October at 1730 UTC).

computations at each time step used the wave field from the previous time step as the initial state.

#### 4.1. Swell Boundary Conditions

[23] Observed estimates of the directional spectrum at site *D* were input uniformly along the open boundaries at each time step. As a sensitivity test the model was also run using the bulk wave statistics ( $H_s$ ,  $T_p$ ,  $\theta_m$ ,  $s_m$ ), which describe only the primary peak, shown in Figure 4. A JONSWAP [Hasselmann *et al.*, 1973] spectral shape with a peak enhancement factor of  $\gamma = 3.3$  was scaled to the bulk wave statistics. A comparison between results based on the directional spectral input and bulk wave statistics input is presented in Figure 6, at a time when two swell peaks (at 0.10 Hz and 0.26 Hz) are entering the bay from different directions (Figure 5a). Although the model does not capture the exact energy level of the primary peak at this time, observations in the bay at *A1* and *A2* show that the secondary swell peak (Figure 6) propagates to those locations. This peak is an important part of the overall wave field, comparable in magnitude to the third spectral peak at 0.45 Hz, locally generated wind sea.

#### 4.2. Wind Input

[24] Accurate wind input is important to the prediction of wind sea. In a coastal area, wind data may be limited

or may be locally affected by topographic sheltering or steering. Winds were observed at three sites in Lunenburg Bay (Figure 2). The wind data, adjusted to 10 m elevation, are shown in Figure 4 for two surface buoys (*P1*, *P2*) and a land-based meteorological station (*W*). The general trends in wind speed and direction are in agreement between the three stations. Differences in wind direction up to  $25^\circ$  exist between *P1*, at the eastern end of the bay, and *W* and *P2*, at the western end (e.g., YD 286.0). These differences in direction lead to differences in fetch of up to 50%, from the shore to each instrument site during the storm.

[25] Estimates of local wave generation in the bay using wind data from *W* at the western end of the bay and *P1* at the eastern end are substantially different. A comparison between spectra using the same model (WN) and winds from each station is shown in Figure 7 at a time of active wave growth. In both runs, the wind data from a single point is used to create a spatially uniform wind field. Site *P1* is geographically closer to the wave observation sites *A1* and *A2*. Surface elevation spectra simulated using winds from *P1* are in much better agreement with the observations at all three locations. The use of winds from *W* results in higher magnitude wind-sea peak, centered at a lower frequency. On the basis of this comparison, wind data from *P1* were chosen as the most representative of winds over

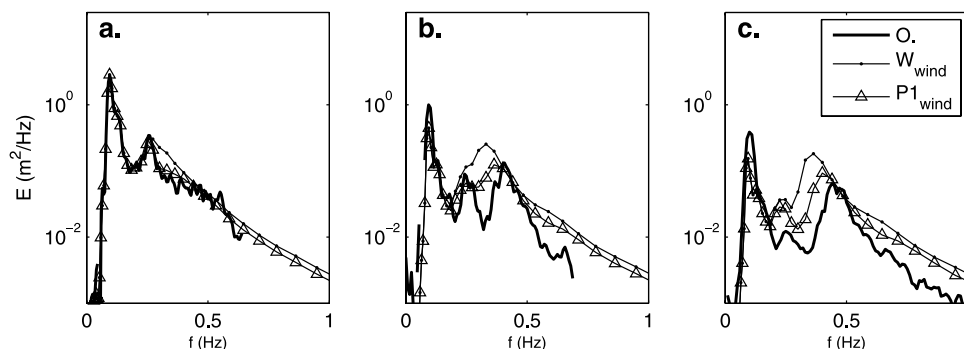


**Figure 7.** Comparison of surface elevation spectra for observations (thick line) and SWAN simulations (WN) using wind data from two different locations, land station *W* and surface buoy *P1*, at (a) site *D*, (b) site *A1*, and (c) site *A2* on YD 285.73 (11 October at 1730 UTC).

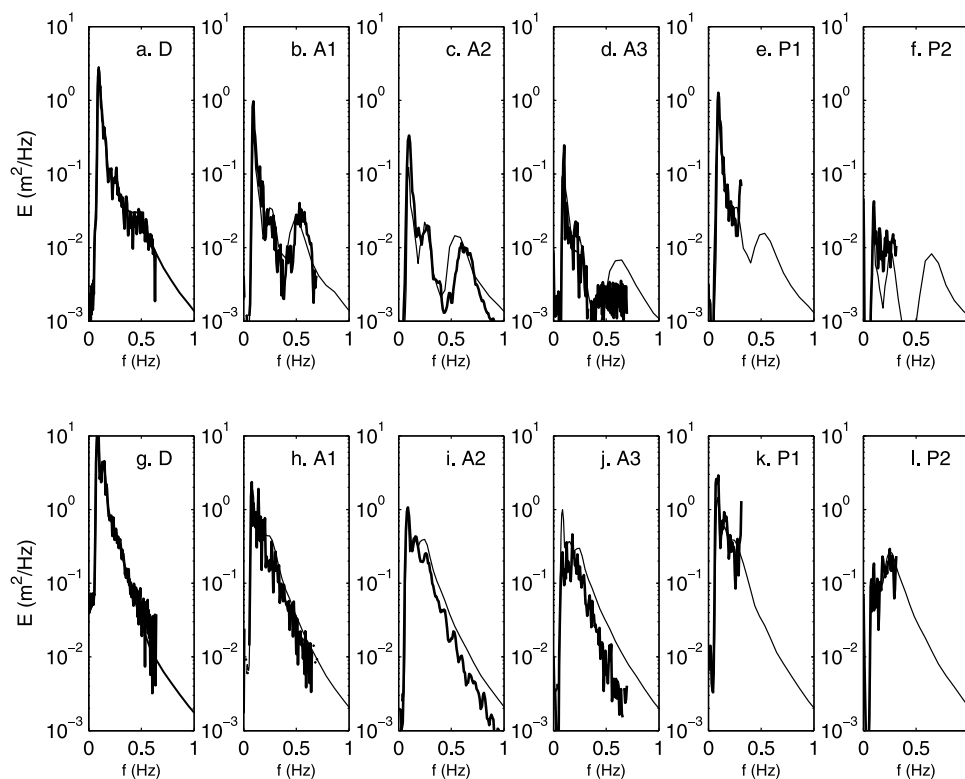


**Figure 8.** Surface elevation spectra at the instrument locations (Figure 2). Observations are shown by the thick lines, SWAN predictions (WN) are shown by the thin lines: (a–f) YD 285.60 (11 October at 1430 UTC) and (g–l) YD 286.64 (12 October at 1530 UTC).

the eastern half of the bay, the area of interest for the wave measurements.

## 5. Comparisons Between Observations and Model Runs

[26] Observed surface elevation spectra at selected times are shown in Figure 8. Model results for run WN are in general agreement with the observations. Figures 8e and 8f illustrate the frequency limit of observations at pressure sensors *P1* and *P2* where the higher frequency wind-sea peak is important. A plot of wave height contours near the time of peak swell conditions is shown in Figure 9 for run WN, showing spatial gradients in wave height that are mainly due to refraction. This is evident in the longitudinal transect, Figure 9b: gradual reduction in wave energy occurs from east to west into the bay, due to the directional spreading of energy. Figure 9b also includes the model results with all dissipation terms turned off. Along the transect the dissipation is dominated by whitecapping, except over a shoal near the west end where bottom friction and breaking are also active. Observations are denoted by open circles on the plot, and model results match the measurements made by acoustic detection of the sea surface (sites *A1*, *A2*), since wind-sea frequencies are included in these observations. The frequency limitation of the pressure sensor observations at sites *P1* and *P2*, which only observed the swell band, agree with model results for  $H_s$  determined from only the swell portion of the wave spectrum.

[27] Extratropical storm Nicole provided an interesting range of wave conditions in Lunenburg Bay. The swell peak attenuated westward into the bay, mainly owing to refraction. The wave spectrum was often bimodal during the storm, and the wind-sea peak often dominated the spectrum in the western part of the bay. The following sections present comparisons between data and the model runs listed in Table 2 for wave statistics (section 5.1), spectra (section 5.2) and source terms (section 5.3) at selected times and locations. Dissipation rates estimated from observations and models are compared in section 5.4.

### 5.1. Bulk Wave Statistics

[28] Wave characteristics such as height and period are often used to describe the overall wave field, as in Figure 3, to indicate the energy levels for wave events with respect to calmer conditions. These bulk parameters are useful in summarizing spectral information, but do not include information regarding spectral shape. Significant wave height  $H_s$  gives an estimate of the total energy, including all spectral peaks. The mean absolute wave period  $T_{m01}$  summarizes the entire spectrum while  $T_p$  selects the period at the energy maximum only, which tends to occur in the lower frequency swell range for the given instrument sites and event conditions. In Lunenburg Bay, peak periods of swell are  $\sim 10$ – $13$  s and wind sea are  $\sim 1$ – $3$  s, which result in mean periods in the 3- to 8-s range.

[29] Time series of  $H_s$  and  $T_{m01}$  for data and model runs are shown in Figure 10 at two observation stations in the bay, *A1* and *A2*. Spin-up time for the nonstationary runs was approx-

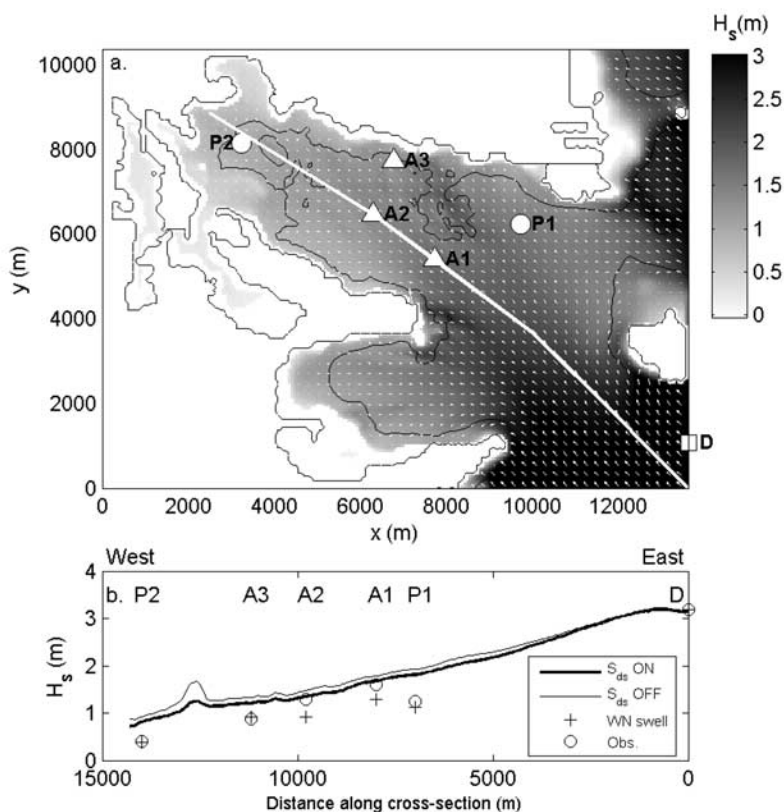


**Figure 9.** Wave conditions on YD 286.64 (12 October at 1530 UTC). (a)  $H_s$  contours and mean direction vectors with boundary input of  $H_s = 3.6$  m using model WN. The 0 m and 10 m bathymetric contours are shown as solid black lines, transect location is denoted by the white line, and instrument locations are shown. (b)  $H_s$  along the transect for the WN model with all dissipation terms ( $S_{ds} = S_{wc} + S_{fr} + S_{br}$ ) on and off. Observations are shown as circles, and model results for swell only are shown as crosses.

imately 3 hours (6 time steps). Differences between KHH84 and WZB07 formulations are apparent, for the mixed sea and swell conditions. The WZB07 runs predict smaller wave height and longer mean period than KHH84 runs. This is caused by stronger whitecapping leading to lower energy and higher frequency of the wind-sea peak, resulting in a longer mean period that is dominated by the swell. Differences between stationary runs (KS,WS) and nonstationary runs (KN,WN) are smaller. However, these differences are important where the curves diverge, indicating periods of time-dependent wave growth coinciding with rapid changes in wind direction. Nonstationary runs are in better agreement with the observations at these times, for example on YD 286.2 and 286.7 when stationary runs overpredict  $H_s$ .

[30] Scatterplots for  $H_s$  and  $T_{m01}$ , comparing nonstationary model runs to the observed data, are shown in Figure 11 for sites  $A1$  and  $A2$ .  $A1$  is more exposed to swell and has a higher  $H_s$ .  $A2$  receives less swell and thus has a higher relative sea-to-swell energy ratio, evident in the lower  $T_{m01}$ . The WN run estimates  $H_s$  and  $T_{m01}$  more accurately than the KN run, shown by the regression coefficient  $\beta$  and correlation statistic  $R^2$  for each run in Figure 11. It is clear that the WZB07 formulation more accurately predicts the bulk wave statistics at both sites. The KHH84 formulation tends to overestimate  $H_s$  and the period of the wind-sea peak, leading to an underestimation of  $T_{m01}$ .

## 5.2. Surface Elevation Spectra

[31] The evolution of sea and swell peaks in the observed energy spectrum at site  $A2$  is shown in Figure 12. Spectra at four selected times are plotted in Figures 13 and 14, together with model predictions. Figures 13a and 14a correspond to the wave buoy ( $D$ ), showing spectra at the entrance to the bay, and SWAN results are shown at one grid cell into the model domain. Figures 13b and 14b and Figures 13c and 14c compare observed and predicted spectra inside the bay at  $A1$  and  $A2$ .

[32] There are no differences in swell propagation or refraction between the model runs. Swell is generally well represented by all four model runs, except at certain times (Figures 13b and 13c) the swell peak magnitude is incorrect, leading to inaccurate  $H_s$  (Figure 10). Above  $\sim 0.3$  Hz, differences between the model runs are due to the different whitecapping source term formulations. The overestimation of the wind-sea peak in the presence of swell using KHH84 is apparent at all times presented in Figures 13 and 14, with corresponding values of  $H_s$  given in Table 3. Percent relative errors with respect to observations are given by

$$RE = \frac{Model - Observation}{Observation} \times 100\%, \quad (9)$$

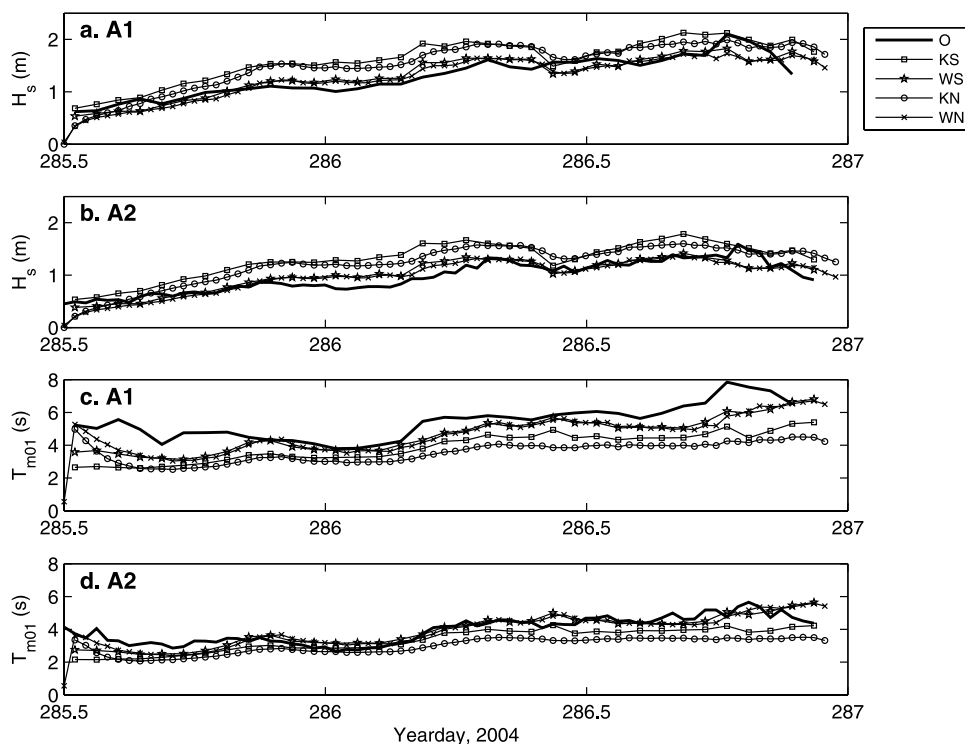


**Figure 10.** Time series of significant wave height ( $H_s$ ) and mean wave period ( $T_{m01}$ ) for observations (O) and model runs: (a)  $H_s$  at site A1, (b)  $H_s$  at site A2, (c)  $T_{m01}$  at site A1, and (d)  $T_{m01}$  at site A2.

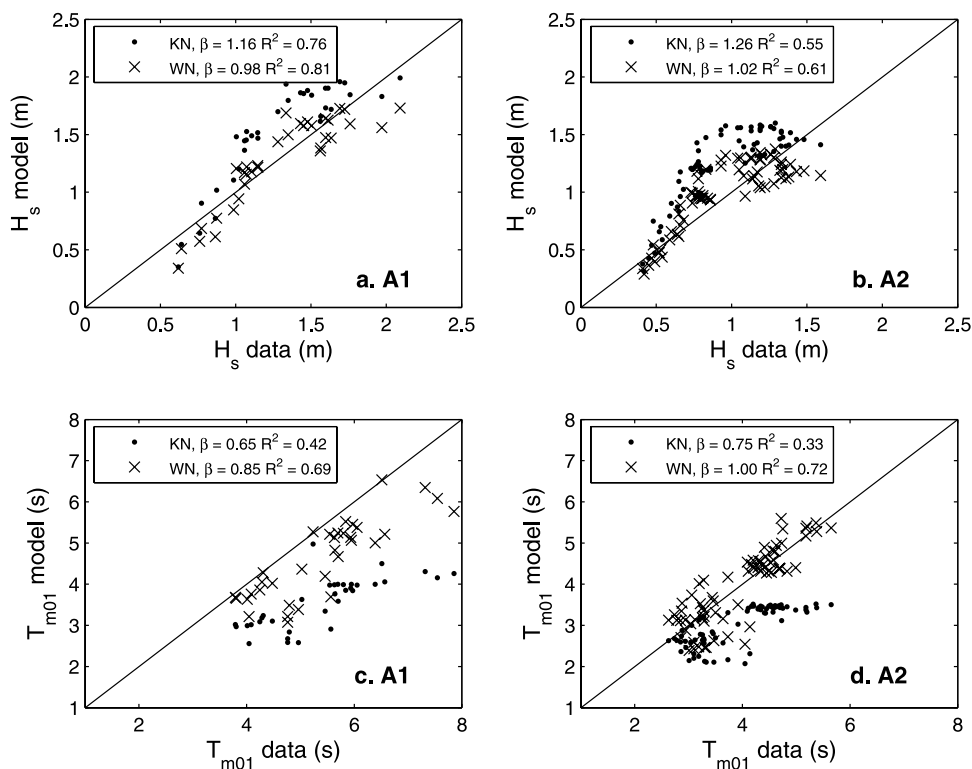


**Figure 11.** Scatterplots of  $H_s$  and  $T_{m01}$  for nonstationary model runs (KN and WN) against data at sites A1 and A2, with linear regression coefficient  $\beta$  and correlation statistic  $R^2$ . The 1:1 line is shown for reference.

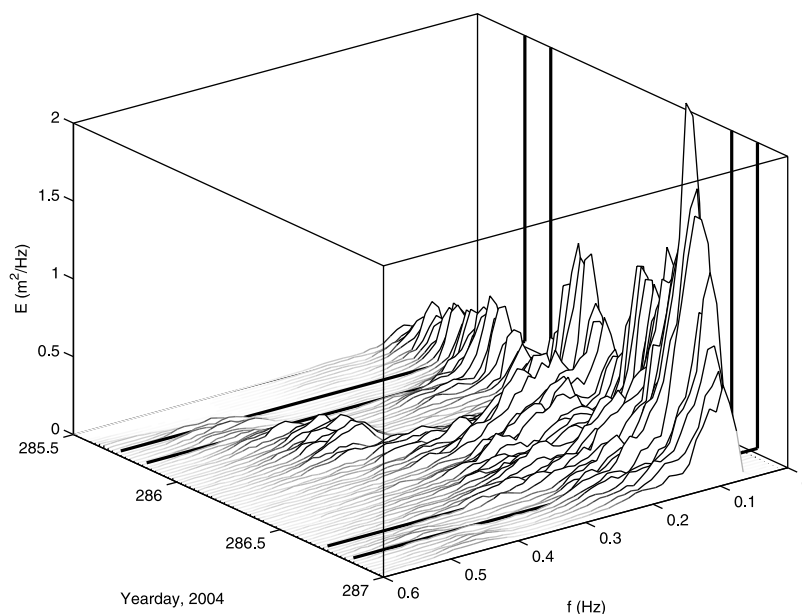


**Figure 12.** Observed surface elevation spectral evolution inside the bay at site *A2* during extratropical storm Nicole. The four thick lines indicate the times selected for Figures 13 and 14.

and are in general much higher (up to  $\sim 50\%$ ) for the KHH84 runs. At YD 286.85, low predictions for  $H_s$  at *A2* is attributed to underestimated swell.

[33] At times were the wind-sea peak is young (Figures 13b, 13c, 14e, and 14f) the importance of time-dependent wave

growth is evident. Stationary runs overpredict the wind-sea peak by computing the wave spectrum with no limit to wind duration. In reality, as shown in observations (Figure 4), wind direction, and thus fetch, are changing rapidly. Non-stationary runs (at  $\Delta t = 30$  min) are much better able to

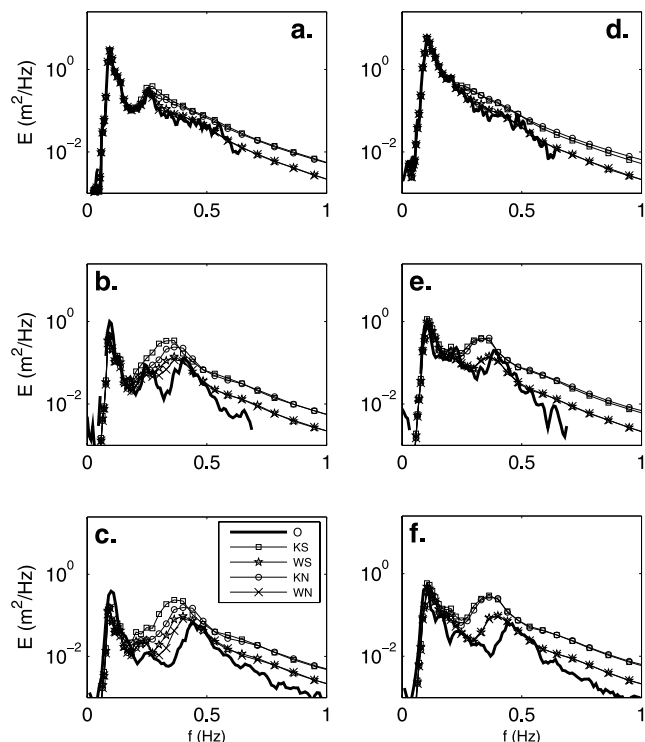


**Figure 13.** Comparison of surface elevation spectra for observations (thick line) and SWAN simulations at three sites: (a) site *D*, (b) site *A1*, and (c) site *A2* on YD 285.73 (11 October at 1730 UTC); (d) site *D*, (e) site *A1*, and (f) site *A2* on YD 285.85 (11 October at 2030 UTC).

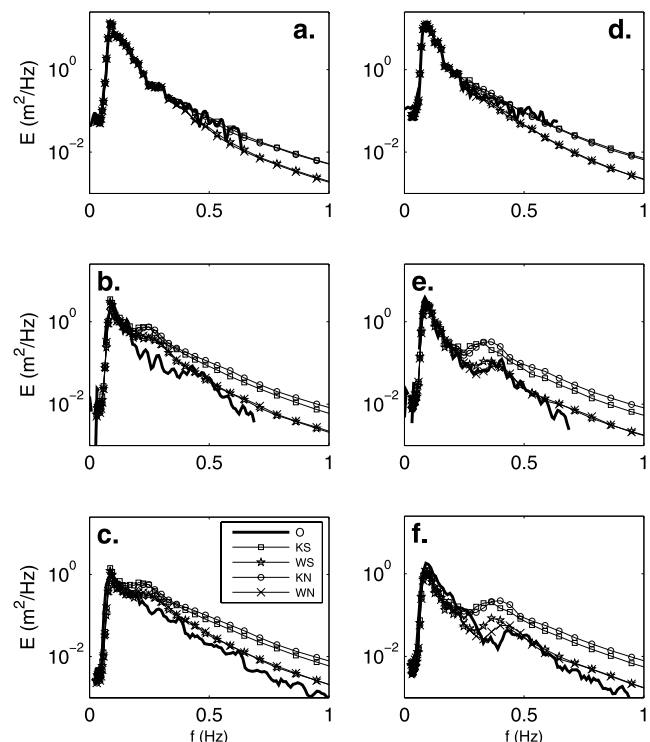


**Figure 14.** Comparison of surface elevation spectra for observations (thick line) and SWAN simulations at three sites: (a) site *D*, (b) site *A1*, and (c) site *A2* on YD 286.73 (12 October at 1730 UTC); (d) site *D*, (e) site *A1*, and (f) site *A2* on YD 286.85 (12 October at 2030 UTC).

**Table 3.** Significant Wave Height and Percent Relative Error for Surface Elevation Spectra Shown in Figures 13 and 14

	YD 285.73	YD 285.85	YD 286.73	YD 286.85
		<i>Site A1</i>		
Observation	0.87 m	1.06 m	1.69 m	1.76 m
KS	1.16 m (+33%)	1.47 m (+39%)	2.09 m (+24%)	1.88 m (+7%)
WS	0.83 m (-5%)	1.12 m (+6%)	1.77 m (+5%)	1.61 m (-9%)
KN	1.02 m (+17%)	1.36 m (+28%)	1.96 m (+16%)	1.85 m (+10%)
WN	0.77 m (-11%)	1.07 m (+1%)	1.73 m (+2%)	1.59 m (-10%)
		<i>Site A2</i>		
Observation	0.64 m	0.74 m	1.33 m	1.48 m
KS	0.92 m (+44%)	1.20 m (+62%)	1.69 m (+27%)	1.41 m (-5%)
WS	0.64 m (+0%)	0.86 m (+16%)	1.33 m (+0%)	1.14 m (-23%)
KN	0.79 m (+23%)	1.09 m (+47%)	1.57 m (+18%)	1.40 m (-5%)
WN	0.59 m (-8%)	0.81 m (+9%)	1.33 m (+0%)	1.13 m (-24%)

simulate the wind-sea peak. Figure 15 shows observed hourly spectra at site *A2*, compared to nonstationary and stationary model results from the WZB07 formulation. Clearly, the stationary model runs are inaccurate over this time period. The stationary run predicts duration-unlimited wave conditions for the given winds, and the modeled spectra reflect the input wind speeds and not the development over time. Stationary and nonstationary computations differ significantly at 1430 UTC (YD 285.60) but after 3 hours both runs agree: adequate duration has allowed the spectra in the nonstationary case to grow to full development for the given wind conditions.

### 5.3. Source Terms and Whitecapping Dissipation Rates

[34] The addition of source terms in SWAN according to equation (5) allows the wave spectrum to be modeled with a balance of input, exchange and dissipation terms. The comparison between model and data in Lunenburg Bay has shown that the WZB07 whitecapping formulation is better than the KHH84 formulation for the event conditions. Breaking down the total modeled spectrum allows for a comparison of the relative magnitudes of source terms that contribute to spectral evolution. In the middle of the bay (site *A2*), sea and swell peaks are similar in magnitude from YD 285.60–285.73. At these times the spectra are trimodal, with two swell peaks entering the model through the open boundary (Figure 13) at 0.10 Hz and 0.26 Hz and a third locally wind-generated peak at 0.45 Hz. Comparing the source terms for nonstationary runs in Figures 16 and 17, the wind-sea peak at

0.45 Hz in the total energy spectrum is much larger for the KHH84 formulation. The magnitudes of individual source terms are drastically different, although only the whitecapping and wind input terms have been changed. Bottom friction ( $S_{fb}$ ) acts only on swell and is the same for both runs. Shallow-water source terms for depth-induced breaking ( $S_{br}$ ) and triad interactions ( $S_{nl3}$ ) are not shown here since they make no contributions to the total ( $S_{tot}$ ) in the location of interest (*A2*, 21 m mean water depth). The wind input term ( $S_{in}$ ) is slightly larger using WZB07, particularly at higher frequencies, from 1 Hz to 3 Hz [Yan, 1987]; however, the whitecapping term ( $S_{wc}$ ) is significantly larger. The combination of  $S_{in}$  and  $S_{wc}$  terms in each run yield different predictions for the strength of quadruplet nonlinear interactions ( $S_{nl4}$ ), using the discrete interaction approximation (DIA) in SWAN. On YD 285.60 (Figure 16) the KHH84 formulation predicts very little whitecapping, while at the same time, whitecapping is a substantial dissipation term using WZB07. At this time, the wind speed was 8.8 m/s, and the lack of whitecapping dissipation results in a stronger  $S_{nl4}$  term. The same phenomenon is noticeable three hours later on YD 285.73 (Figure 17) when the wind speed was stronger at 13.8 m/s. Stronger  $S_{wc}$  in the WZB07 run reduces the  $S_{nl4}$  term and  $S_{tot}$  (when compared to KHH84) resulting in a spectral shape and magnitude that better matches observations (Figure 13c). The cumulative effects over time in the nonstationary run lead to an overprediction of the wind-sea portion of the spectrum by KHH84, when swell is present.

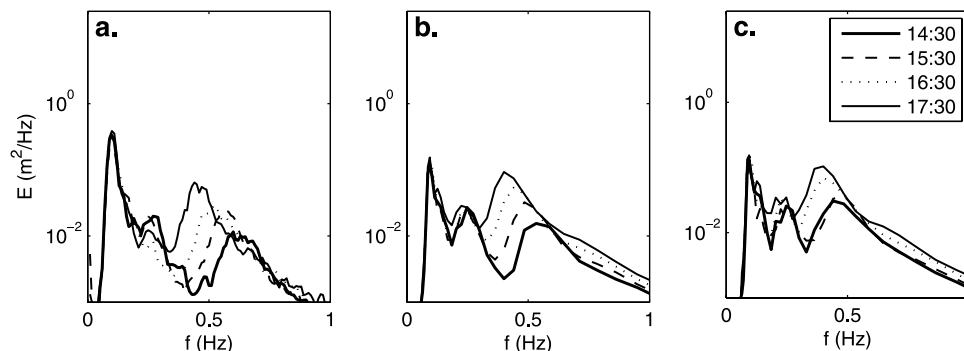


**Figure 15.** Hourly comparison of wind-sea growth at site *A2* at selected times on 11 October 2004 (YD 285.60 to 285.73) using the WZB07 formulation: (a) observations, (b) nonstationary computations, and (c) stationary computations.

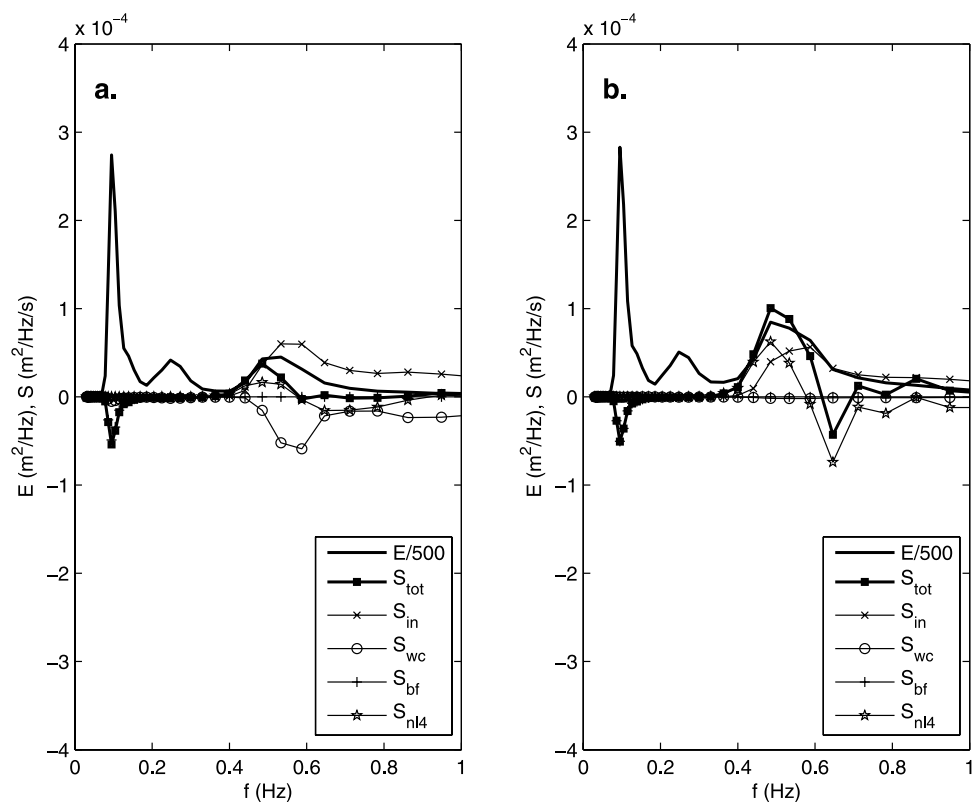


**Figure 16.** Wave energy spectra and source terms from nonstationary runs at site *A2*, YD 285.60. (a) WZB07 formulation and (b) KHH84 formulation.

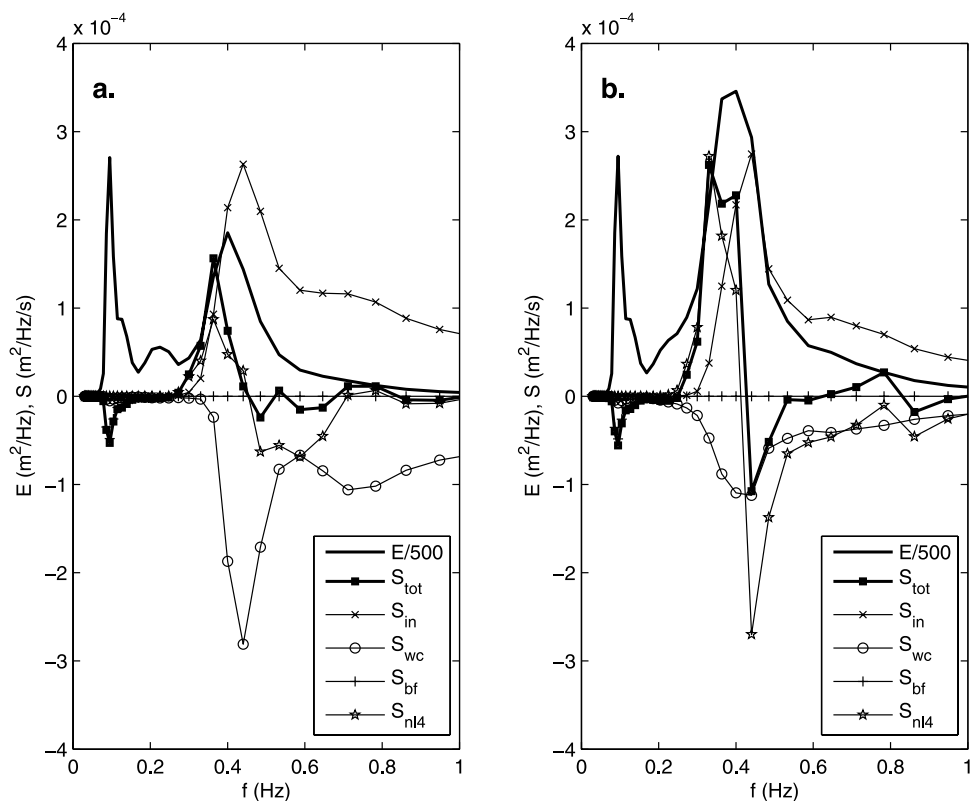


**Figure 17.** Wave energy spectra and source terms from nonstationary runs at site *A2*, YD 285.73. (a) WZB07 formulation and (b) KHH84 formulation.

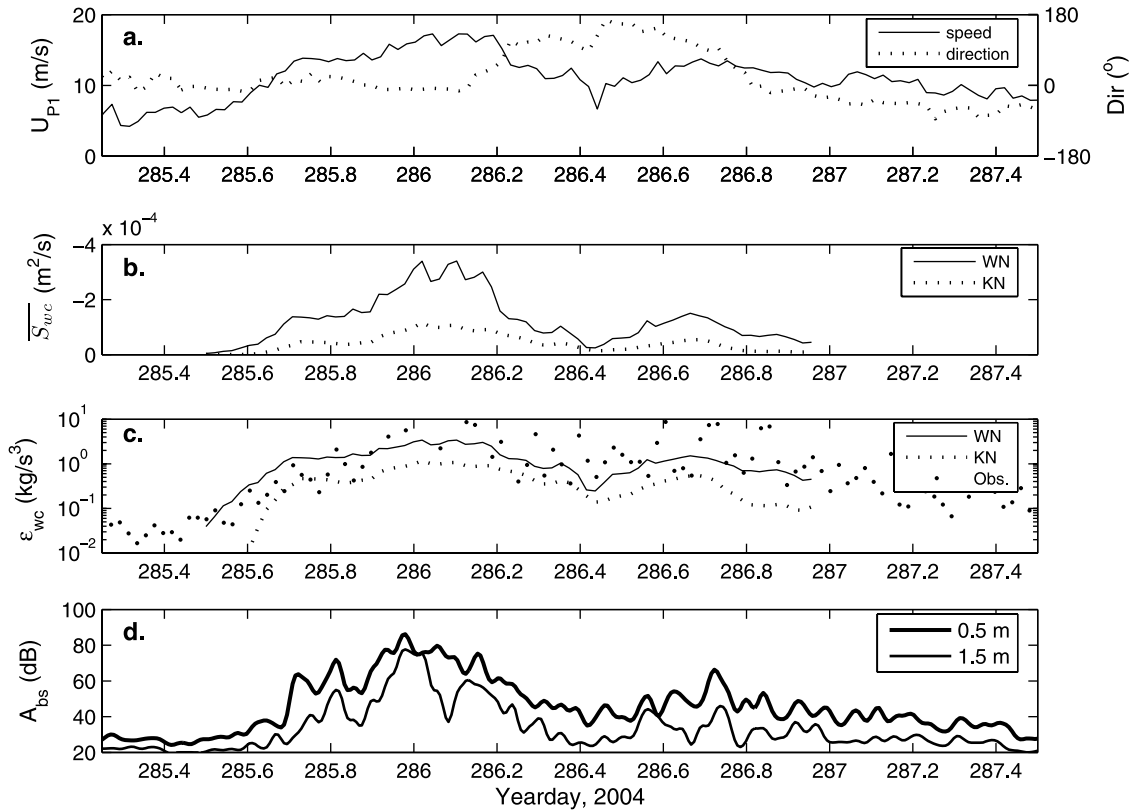


**Figure 18.** Time series of whitecapping dissipation rate estimates compared to wind forcing and acoustic backscatter observations: (a) wind speed adjusted to 10 m elevation and wind direction in degrees relative to true north at surface buoy  $P1$ , (b) frequency-integrated whitecapping source term estimates at  $A2$  from WZB07 and KHH84 formulations in SWAN, (c) whitecapping dissipation rates estimated at  $A2$  by models and observations using equilibrium range theory, and (d) three-beam mean near-surface acoustic backscatter observations at  $A2$ .

[35] Having shown that modeled surface elevation spectra match observations (section 5.2), what surface wave energy dissipation rates occurred for the conditions observed in Lunenburg Bay? To answer this we integrate the whitecapping term over all frequencies:

$$\overline{S_{wc}} = \int S_{wc}(\sigma) d\sigma, \quad (10)$$

and change units from  $m^2/s$  to  $kg/s^3$  via

$$\epsilon_{wc} = \rho g \overline{S_{wc}}. \quad (11)$$

Figure 18 presents wind conditions and model estimates of  $\overline{S_{wc}}$  and  $\epsilon_{wc}$  over the simulation period, and shows that KHH84 predicts significantly lower dissipation than WZB07. For winds in the 5 to 17 m/s range,  $\epsilon_{wc}$  is estimated to be 0.1–3.0  $kg/s^3$  using WZB07, approximately 3 times higher than using KHH84. In the next section, dissipation rate estimates from observations are described and compared to the model results.

#### 5.4. Observed Dissipation Rates

[36] Proposed by *Phillips* [1985], equilibrium range theory describes the balance of forcing, dissipation and transfer terms that make up the wave spectrum above the peak

frequency for wind-sea  $\sigma_p$ . The equilibrium spectrum is given by

$$E(\sigma) = \alpha u_* g \sigma^{-4}, \quad (12)$$

where  $\alpha$  is the Toba coefficient and  $u_*$  is the friction velocity. *Phillips* [1985] derived the wave energy dissipation rate  $\epsilon$ ,

$$\epsilon = \frac{\rho \gamma I(3p)}{16 [I(p)]^3 g^3} \int_{\sigma_p} \sigma^{11} E(\sigma)^3 d\sigma, \quad (13)$$

where  $I(p)$  is a spreading function

$$I(p) = \int_{-\pi/2}^{\pi/2} (\cos \theta)^p d\theta, \quad (14)$$

with  $p$  typically ranging from 0.5 to 2.0, and  $\gamma$  is given by

$$\gamma \approx 0.04 \left( \frac{\alpha}{4I(p)} \right)^{-2}. \quad (15)$$

Values for  $\alpha$  typically range from 0.06 to 0.11 [*Phillips*, 1985], and have been shown in later studies to be closer to 0.11 [*Felizardo and Melville*, 1995; *Hanson and Phillips*,

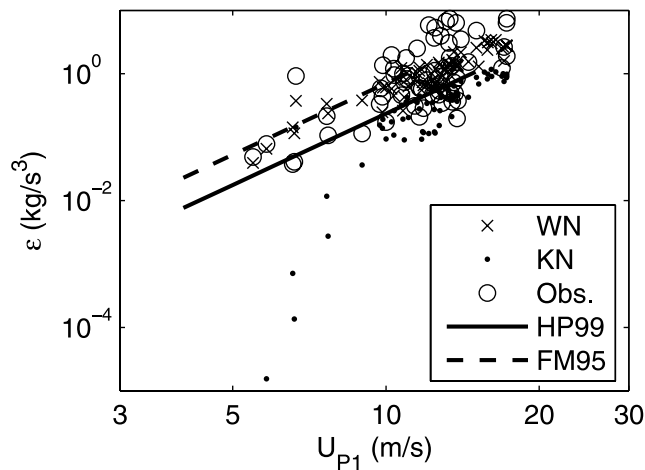


**Figure 19.** Wave energy dissipation rate estimates from models and observations at *A2* from YD 285.5–287.0 with wind speed at P1. Relationships developed by *Hanson and Phillips* [1999] and *Felizardo and Melville* [1995] are shown as lines.

1999]. In the present study, observed surface elevation spectra up to 2 Hz at site *A2* are in agreement with  $\alpha = 0.11$ . Assuming wider directional spreading for a young sea, wave energy dissipation rates have been estimated from the observations using equation (13) with  $p = 0.5$ . The estimates are shown in Figure 18c. The observed dissipation rates are scattered, but in general follow the pattern predicted by SWAN and are in closer agreement with the higher values predicted with WZB07.

[37] A comparison of the present rates to those of *Hanson and Phillips* [1999] and *Felizardo and Melville* [1995] is shown in Figure 19. *Hanson and Phillips* [1999] investigated wind-sea growth and whitecapping dissipation in a swell-dominated, open ocean environment in the Gulf of Alaska. *Felizardo and Melville* [1995] estimated correlations between wind and wave parameters off the coast of Oregon in 3000 m water depth. Both used the equilibrium range theory of *Phillips* [1985] to estimate dissipation rates, although *Hanson and Phillips* [1999] replaced the directional spreading function  $I(p)$  with observed directional spectra. Their results are shown as lines on Figure 19, together with the observed and model predicted rates from the present study. The Lunenburg Bay observations are scattered, but demonstrate a similar relationship between  $\epsilon$  and  $U_{10}$ . For winds from 5 to 17 m/s, dissipation rates are 0.1–10 kg/s<sup>3</sup>. The stronger model-predicted dissipation rates using WZB07 agree with the previous studies and are in better agreement with *Felizardo and Melville* [1995] for similar wind speeds, despite large differences in fetch for each case. At wind speeds under 10 m/s, failure of KHH84 is apparent. The dissipation is several orders of magnitude too low, evidence of the weighting of swell on the spectral-mean wave number in the formulation.

[38] The acoustic instruments used in this study also provide measurements of backscatter intensity. Observed acoustic backscatter, in decibels sound pressure, at 0.5 and 1.5 m below the mean water surface are presented in Figure 18d. The backscatter is strong, well-correlated with wind speed, and is significantly reduced at times when wind

direction changes rapidly (Figure 18a). As wind speed increases, whitecapping becomes stronger and bubbles are injected into the water column from breaking waves. Backscatter measurements act as a proxy for the total concentration of scatters in the water, demonstrating the correlation between near-surface bubbles and the dissipation rate. The near-surface backscatter serves to confirm the occurrence and temporal variations in whitecapping.

## 6. Conclusions

[39] Wave observations collected in Lunenburg Bay, Nova Scotia, have allowed for the physical validation of a new whitecapping source term that attempts to properly represent the dissipation process in the SWAN model. The surface wave observations were made using a directional wave buoy, three acoustic wave instruments and two pressure sensors during an extratropical storm. The storm provided a combination of sea and swell conditions, with offshore significant wave heights reaching 3.8 m and peak periods over 10 s. Wind conditions were time-varying and wind directions changed with the passage of the storm center, resulting in fetch limitations and duration limitations to the growth of local wind sea. Significant differences in wave model results were attained when using spatially uniform wind fields developed from different observation sites. The differences in fetch, due to differences in wind direction between observation sites, illustrate that the spatial variability of coastal winds must be considered carefully when predicting locally generated wind sea. Wind-sea conditions can dominate the wave field in semiprotected coastal areas during storms. Nonstationary computations were better than stationary computations for modeling local wind-generated wave growth when strong changes to wind speed and direction occur over timescales of less than 3 hours. The model run that combined nonstationary computations and the *van der Westhuysen et al.* [2007] whitecapping formulation provided the closest agreement with observed wave data at several locations, for the mixed sea and swell conditions that occurred during the storm.

[40] The two whitecapping formulations compared in this paper have different underlying physics: either the whitecapping process is dependent on the spectrally averaged wave number or the spectrally local wave number. Thus either swell has a major influence on dissipation of wind sea, or very little. It has been shown, by comparison with observations, that better model results are obtained when the influence of swell on whitecapping is neglected. The *van der Westhuysen et al.* [2007] (spectrally local) whitecapping formulation reproduced the magnitude and shape of the wind-sea spectral peak in the presence of swell much better than the *Komen et al.* [1984] (spectrally averaged) formulation. In fact, defining the whitecapping process by including spectrally averaged wave properties significantly underestimated the dissipation, leading to overpredicted wave energy by up to 50% that had implications on other source terms. The spectrally local whitecapping dissipation rates were in agreement with the estimates made from observations by using *Phillips* [1985] equilibrium range theory, and were estimated to be 0.1–10 kg/s<sup>3</sup> for wind speeds from 5 to 17 m/s. Dissipation rates estimated with the spectrally local expression compare very well to the

observations of both *Hanson and Phillips* [1999] and *Felizardo and Melville* [1995] for similar wind conditions, providing additional physical validation for the new source term. Other forms of coupling between swell and wave growth/dissipation, such as the influence of swell on atmospheric boundary layer thickness, are expected to be of secondary importance and could be included in wave models as separate source terms.

[41] **Acknowledgments.** We would like to thank Doug Schillinger at Dalhousie for setup, deployment, and recovery of two of the acoustic instruments. We are grateful to Peter Smith at the Bedford Institute of Oceanography for cooperation and sharing of directional waverider and acoustic data. We would also like to thank Eric Siegel of NortekUSA for providing the AWAC. This study was supported by the Canadian Foundation for Climate and Atmospheric Sciences and the Natural Sciences and Engineering Research Council of Canada.

## References

- Alves, J., and M. Banner (2003), Performance of a saturation-based dissipation-rate source term in modelling fetch-limited evolution of wind waves, *J. Phys. Oceanogr.*, *33*, 1274–1298.
- Booij, N., R. Ris, and L. Holthuijsen (1999), A third-generation wave model for coastal regions: 1. Model description and validation, *J. Geophys. Res.*, *104*, 7649–7666.
- Booij, N., L. Holthuijsen, and J. Battjes (2001), Ocean to near-shore wave modelling with SWAN, paper presented at Fourth Conference on Coastal Dynamics, Am. Soc. of Civ. Eng., Lund, Sweden.
- Dupont, F., C. Hannah, D. Greenberg, J. Cherniawsky, and C. Naimie (2002), Modelling system for tides, *Can. Tech. Rep. Hydrogr. Ocean Sci.*, *221*, 72 pp.
- Felizardo, F., and W. Melville (1995), Correlations between ambient noise and the ocean surface wave field, *J. Phys. Oceanogr.*, *25*, 513–532.
- Hanson, J., and O. Phillips (1999), Wind sea growth and dissipation in the open ocean, *J. Phys. Oceanogr.*, *29*, 1633–1648.
- Hasselmann, K., et al. (1973), Measurements of wind-wave growth and swell decay during the Joint North Sea Wave Project (JONSWAP), *Dtsch. Hydrogr. Z.*, *8*(A12), 95 pp.
- Komen, G., S. Hasselmann, and K. Hasselmann (1984), On the existence of a fully developed wind-sea spectrum, *J. Phys. Oceanogr.*, *14*(8), 1271–1285.
- Krogstad, H. (1991), Reliability and resolution of directional wave spectra from heave, pitch, and roll data buoys, in *Directional Ocean Wave Spectra*, edited by R. Beal, pp. 66–71, Johns Hopkins Univ. Press, Baltimore, Md.
- Lygre, A., and H. Krogstad (1986), Maximum entropy estimation of the directional distribution of ocean wave spectra, *J. Phys. Oceanogr.*, *16*, 2052–2060.
- Ou, S., J. Liao, T. Hsu, and S. Tzang (2002), Simulating typhoon waves by SWAN wave model in coastal waters of Taiwan, *Ocean Eng.*, *29*, 947–971.
- Phillips, O. (1985), Spectral and statistical properties of the equilibrium range in wind-generated gravity waves, *J. Fluid Mech.*, *156*, 505–531.
- Ris, R., L. Holthuijsen, and N. Booij (1999), A third-generation wave model for coastal regions: 2. Verification, *J. Geophys. Res.*, *104*, 7667–7681.
- Rogers, W., P. Hwang, and D. Wang (2002), Investigation of wave growth and decay in the SWAN model: three regional-scale applications, *J. Phys. Oceanogr.*, *33*, 366–389.
- Rogers, W., J. Kaihatu, L. Hsu, R. Jensen, J. Dykes, and K. Holland (2006), Forecasting and hindcasting waves with the SWAN model in the Southern California Bight, *Coastal Eng.*, *54*, 1–15.
- Sheng, J., and L. Wang (2004), Numerical study of tidal circulation and nonlinear dynamics in Lunenburg Bay, Nova Scotia, *J. Geophys. Res.*, *109*, C10018, doi:10.1029/2004JC002404.
- Snyder, R., F. Dobson, J. Elliot, and R. Long (1981), Array measurements of atmospheric pressure fluctuations above surface gravity waves, *J. Fluid Mech.*, *102*, 1–59.
- Sturley, D., and A. Bowen (1996), A model for contaminant transport in Lunenburg Bay, Nova Scotia, *Sci. Total Environ.*, *179*, 161–172.
- van der Westhuysen, A., M. Zijlema, and J. Battjes (2007), Nonlinear saturation-based whitecapping dissipation in SWAN for deep and shallow water, *Coastal Eng.*, *54*, 151–170.
- Yan, L. (1987), An improved wind input source term for third generation ocean wave modelling, *Tech. Rep. 87-8*, 10 pp., R. Dutch Meteorol. Inst., De Bilt, Netherlands.

J. A. Battjes, Environmental Fluid Mechanics Section, Faculty of Civil Engineering and Geosciences, Delft University of Technology, P.O. Box 5048, NL-2600 GA Delft, Netherlands. (j.a.battjes@tudelft.nl)

A. J. Bowen, A. E. Hay, and R. P. Mulligan, Department of Oceanography, Dalhousie University, 1355 Oxford Street, Halifax, NS, Canada B3H 4J1. (tony.bowen@phys.ocean.dal.ca; alex.hay@phys.ocean.dal.ca; mulligan@phys.ocean.dal.ca)

A. J. van der Westhuysen, WL|Delft Hydraulics, P.O. Box 177, NL-2600 MH Delft, Netherlands. (andre.vdwesthuysen@wldelft.nl)